Geoscience Letters

REVIEW

Open Access

Methods to derive the magnetopause from soft X-ray images by the SMILE mission

Chi Wang[1,2*] and Tianran Sun[1*]

Abstract

Solar wind Magnetosphere Ionosphere Link Explorer (SMILE) is a novel self-standing mission dedicated to observing the solar wind–magnetosphere coupling via simultaneous in situ solar wind/magnetosheath plasma and magnetic field measurements, soft X-ray images of the magnetosheath and polar cusps, and UV images of global auroral distributions. While analyzing the observed images after the launch of SMILE, it will be a challenging task to reconstruct the 3-dimensional surface of the magnetopause from 2-dimensional images. Therefore, one of the most important key issues about SMILE is the reconstruction of magnetopause from X-ray images. This paper will review four main approaches have been developed so far, namely, the boundary fitting approach (BFA), the tangent fitting approach (TFA), the tangential direction approach (TDA), and the computed tomography approach (CTA). We will discuss their scope of application and pros and cons, and hopefully inspire future efforts.

Keywords: Solar wind–magnetosphere interaction, Soft X-image, Magnetopause

Introduction

The solar wind is a stream of charged particles (protons, electrons, and heavier ionized atoms) released from the outer atmosphere of the Sun. Near Earth, the solar wind encounters the Earth's magnetic filed, carving a cavity known as the magnetosphere. The solar wind compresses the sunward side of the magnetosphere, but drags the nightside out into a long magnetotail. The interaction of the solar wind with Earth's magnetosphere leads to the formation of large-scale plasma structures, including the bow shock, magnetosheath, magnetopause, cusps, and magnetotail. The collisionless bow shock stands upstream in the supersonic solar wind flow. The magnetopause is a relatively sharp transition layer (interface) between dense shocked, highly ionized solar wind plasma and the tenuous, less highly ionized magnetospheric plasma.

The interaction between the solar wind and the Earth's magnetosphere, and the geospace dynamics that result, is one of the key questions in plasma physics. In order to understand and predict the effect of the solar activities on the geospace environment, we need to understand and model the processes governing the flow of solar wind mass, momentum, and energy through the solar wind magnetosphere–ionosphere system. A host of mechanism have been proposed to explain the nature of the solar wind–magnetosphere interaction, and in particular the solar wind mass and energy entry into the magnetosphere (see, e.g., Russell 2000, for a review). Proposed magnetopause entry mechanisms include magnetic reconnections, Kelvin–Helmholtz instability on the magnetopause, diffusion driven by wave–particle interactions, etc. The position and shape of the magnetopause and cusps change constantly as the Earth's magnetosphere responds to varying solar wind dynamic pressures and interplanetary magnetic field orientations. Both the fast and slow solar wind can be interrupted by large, fast-moving bursts of plasma called interplanetary coronal mass ejections (ICMEs). When an ICME impacts the Earth's magnetosphere, it temporarily deforms the Earth's magnetic field, changing its direction and strength, and inducing

*Correspondence: cw@spaceweather.ac.cn; trsun@spaceweather.ac.cn

[1] State Key Laboratory of Space Weather, National Space Science Center, CAS, Beijing, China
Full list of author information is available at the end of the article

large electrical currents; this is called a geomagnetic storm and it is a global phenomenon. The southward interplanetary magnetic fields, as presented in some ICME events, could produce magnetic reconnection in the Earth's magnetotail; this launches protons and electrons downward toward the Earth's atmosphere, where they result in the aurora. The stored energy in the magnetotail is intermittently and explosively released, and is associated with bright auroral displays in polar regions, which is called substorm (see, e.g., Akasofu 1985, for a review).

A fleet of solar wind and magnetospheric constellation missions now provide the most detailed observations of solar wind–magnetic interaction. In situ data have dramatically improved our understanding of the localized physical processes involved. Missions such as NASA's Magnetospheric Multi-Scale mission proceed down this path with an ever-increasing focus on the microscopic physics of space plasmas. However, piecing the individual parts together to make a coherent overall picture, capable of explaining and predicting the dynamics of the magnetosphere at the system level has proved to be extremely difficult. This is due to the fact that it is fundamentally impossible to determine the global behavior of a complex system with sparse in situ measurements, even with the support of increasingly sophisticated global numerical models. The remote sensing of the cusps and magnetosheath with X-ray imaging is now possible (Collier et al. 2012) thanks to the relatively recent discovery of the solar wind charge exchange (SWCX) X-ray emission (see Sibeck et al. 2018, for a review). The global information about the magnetosphere is the key missing link in understanding of how the solar wind gives rise to and controls Earth's plasma environment and space weather.

The Solar wind Magnetosphere Ionosphere Link Explorer (SMILE) mission is a joint European Space Agency (ESA) and Chinese Academy of Sciences (CAS) mission (SMILE science study team 2018; Wang and Branduardi-Raymont 2018). It is a novel self-standing mission dedicated to observing the solar wind–magnetosphere interaction via simultaneous, soft X-ray images of the magnetosheath and polar cusps, UV images of global auroral distributions, and in situ solar wind/magnetosheath plasma and magnetic field measurements. It aims to measure Earth's global system responses to solar wind and geomagnetic variations. The scientific payloads on board SMILE include the Soft X-ray Imager (SXI), Ultra-Violet Imager (UVI), Light Ion Analyzer (LIA), and the Magnetometer (MAG). Following the recommendation of the joint ESA–CAS scientific evaluation panel, SMILE was selected in November 2015, with a target launch date by end of 2024. The mission was adopted by CAS in November 2016 and by ESA in March 2019. It is the first time that ESA and China jointly select, design, implement, launch and operate a space mission.

SMILE will adopt a highly elliptical orbit with an apogee of 19 Re, a perigee of 5000 km, and a period of 51 h. The inclination will be 70 ° or 98 ° depending on the launch vehicle (VEGA-C or Arian 6) to be decided later, with the VEGA-C launch option as the design baseline. Figure 1 shows the sketch of the orbital and viewing geometry of SMILE. The black thick ellipse is an example of an orbit, black thin lines depict the magnetopause and bow shock. SMILE's SXI can be used to determine the nature of the dayside solar wind–magnetosphere interaction from conditions prevailing at the Earth's bow shock, magnetopause, and cusps. While analyzing the observed images after the launch of SMILE, it will be a challenging task to extract 3D information of the dayside boundaries such as bow shock, magnetopause, low- and high-latitude cusp boundaries from soft X-ray images, since these 2D images are basically line-of-sight integrations of soft X-ray emissions. This paper will review the reconstruction techniques that have been developed so far, discuss the pros and cons of each approach, and hope to inspire future direction to develop more realistic and robust reconstruction approaches.

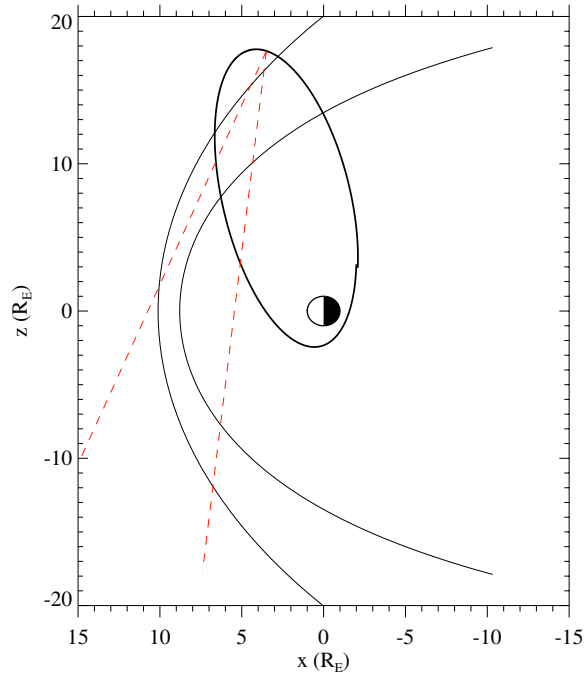

Fig. 1 The SMILE orbit. A sketch of the orbital and viewing geometry of the Solar wind Magnetosphere Ionosphere Link Explorer (SMILE) mission. The coordinates are in Earth radii. The x-axis points toward the Sun in the left. The black thick ellipse is a example of an orbit, black thin lines depict the magnetopause and bow shock

A review of methods

Solar wind charge exchange (SWCX) occurs when highly ionized species in the solar wind interact with neutral atoms such as the exospheric (geocoronal) hydrogen. SWCX was first proposed by Cravens (1997) to explain observations of X-ray emissions from the comet. An electron from the neutrals is transferred to the ion initially in a highly excited state, for example O^{6+}, O^{7+}, C^{5+}, etc. On relaxation to the ground state one or more photons are emitted, producing soft X-ray of 0.5–2.0 keV band. These highly ionized solar wind ions originate in the solar atmosphere, and, for the most part, do not enter the magnetospheric cavity (magnetosphere) and thus are mainly present in the magnetosheath and cusps. Earth's atmosphere does not contain highly ionized ions due to its lower temperature. Therefore, soft X-ray emissions mainly come from outside of the magnetopause, and rarely from the inside of the magnetopause, creating a sharp boundary.

The SMILE SXI is a widefield lobster-eye telescope equipped with CCD detectors, developed by the University of Leicester, UK. The latest design of the SXI has a field of view of 16^o by 27^o. It will perform soft X-ray observations of the subsolar magnetopause and cusps. The soft X-ray flux is given by the integral of $P = \alpha_{cx} n_H n_{sw} V_{rel}$ along the line of sight, where α_{cx} is an efficiency factor dependent on the ion abundance, interaction cross-sections, branching ratios, etc. Typical value for α_{cx} is about 6×10^{-16} to 6×10^{-15} (Cravens 2000). n_H is the density of neutral particles, usually estimated as $25(\mathrm{cm}^{-3})(10(R_E)/r)^3$ (Cravens et al. 2001). n_{sw} is the density of solar wind protons with typical values as 5–12 cm^{-3} (Wilson et al. 2021), and V_{relv} is their relative velocities typically several hundred km/s. The SXI will basically take 2D soft X-ray image of the intended target, with its FOV keeping changing as the spacecraft moves along orbit. It is essential to identify the exact location of the magnetopause, and will be a challenging task to to reconstruct the 3-dimensional surface of the magnetopause from 2-dimensional images.

So far, four approaches have been developed to derive the 3-D magnetopause position from X-ray images, namely the tangential direction approach (TDA), boundary fitting approach (BFA), tangent fitting approach (TFA), and computerized tomography approach (CTA). They will be introduced in the following sub-sections.

Tangential direction approach (TDA)

The tangent vector plays a central role in differential geometry, which can be used to define global geometry of the magnetopause. Under a broad range of conditions, the peak soft X-ray emission corresponds to the tangent to the boundary surface such as magnetopause, the so-called limb brightening phenomenon (Collier et al. 2014). The viewing angle that touches the edge of the magnetopause has the longest path length through the emission region in the magnetosheath (Collier and Connor 2018). More emission occurs along this direction, producing a bright edge.

To determine the validity of the assumption that the local peaks in the observed SWCX soft X-ray flux coincide with the line-of-sight tangents to the magnetopause, Collier and Connor (2018) performed MHD simulations using OpenGGCM (e.g., Raeder et al. 2008). The MHD models were run and then line-of-sight integrations were calculated to determine the total soft X-ray flux observed in that direction due to the solar wind SWCX with exospheric neural hydrogen. Figure 2 shows an example of the results from MHD simulation for a southward interplanetary magnetic field (IMF) of 5 nT, a solar wind density of 10 cm^{-3}, and a flow speed of 400 km s^{-1}. In this case, the spacecraft was orbiting in the geocentric solar ecliptic (GSE) *YZ* plane (GSE $X = 0$). The top left panel in Fig. 2 shows the local soft X-ray emission at each point in this plane, and the top right panel shows the plasma density. Although densities peak in the outermost magnetosheath, emissions peak in the inner magnetosheath, since the total observed soft X-ray intensity depends not only on plasma density, but also on the exospheric neutral density and effective velocity. The lines in these two panels originate at the spacecraft location and show both the direction of the local peak in the soft X-ray emission (black) and the direction of the tangent to the magnetopause location (red). The lower panel in Fig. 2 shows that the direction of the peak emission (θ_{XR}) and the direction tangent to the magnetopause (θ_{MP}) coincide to each other with an accuracy higher than one degree by plotting the line-of-sight integrated emission versus the line-of-sight angle. As expected, the difference between the two angles increases as the observation point gets closer to Earth. This appears to be a general property, namely, that a local peak in the observed soft X-ray flux occurs coincident with the geometric tangent line of sight to the surface.

To derive the general formula for reconstruction of the magnetopause from the spacecraft position, $\vec{s}$, parameterized by tangent angle θ, Fig. 3 illustrates the geometry. The point **O** is an arbitrary origin, $\vec{r}$ is the line-of-sight tangent direction unit vector, $\vec{s}$ is the vector define the spacecraft (for example, SMILE) location relative to **O**, θ is the observed angle between the line-of-sight tangent and the positive x direction. As derived by Collier and Connor (2018), the general formula is:

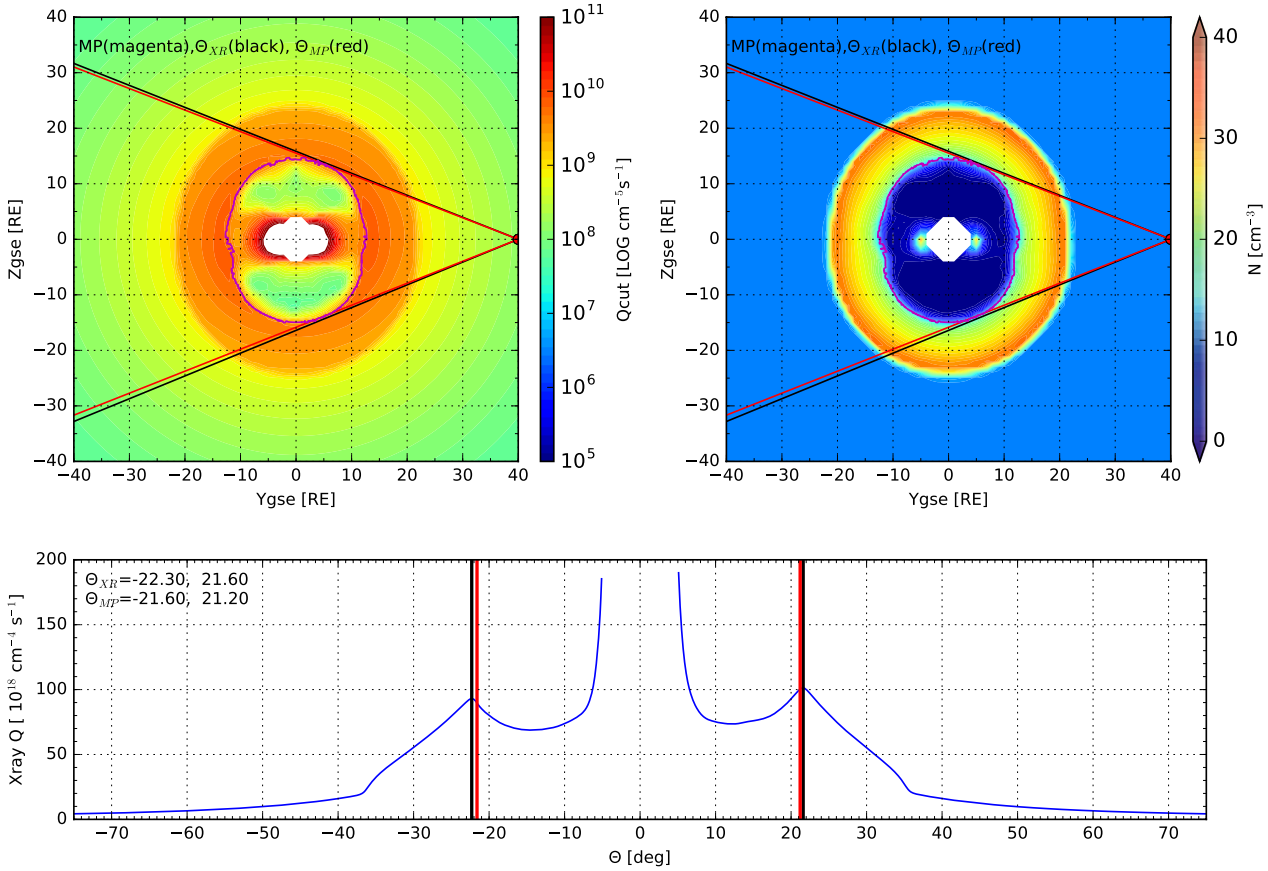

Fig. 2 Tangent direction of the magnetopause. Correspondence between the peak soft X-ray emission and the tangent to the magnetopause. The magnetopause is taken to correspond to the maximum plasmas density gradient (Figure adapted from Collier and Connor (2018))

$$\vec{p} = \left| \frac{d\vec{s}}{d\theta} \cdot \hat{\theta} \right| \vec{r} + \vec{s}. \tag{1}$$

The magnetopause location can then be determined by the derivative of the spacecraft position with respect to the angle of the tangent direction.

Figure 4 shows the application of the reconstruction algorithm to a case in which the spacecraft executes a circular orbit in the GSE YZ plane of 20 Re radius (black). The top panel shows the relationship between the spacecraft location, and the angle at which the maximum soft X-ray flux is observed (θ). The middle panel shows $|ds/d\theta|$, the derivative of the spacecraft position with respect to the observation angle of peak soft X-ray intensity. The bottom panel shows the magnetopause reconstruction resulting from the soft X-ray emission simulation (red, blue, and green) using equation 1 superimposed on the MHD plasma density results (shading). The black and yellow lines indicate the spacecraft orbit and the magnetopause locations calculated from the MHD model, respectively. The algorithm reconstructs the magnetopause location with reasonable accuracy. The root-mean-square (rms) difference between the position of the magnetopause based on the MHD simulation and the position calculated from the reconstruction algorithm is about 0.18 Re. In fact, the reconstruction algorithm manages to even reproduce the outer cusp shape viewing from satellite positions in the XZ plane (not shown here).

There are, however, limitations inherent in this reconstruction approach, for example, the assumption of time stationarity and the offset between the peak density gradient and the maximum soft X-ray emission. The first limitation could be alleviated by orbit binning the data according the desired solar wind conditions and then reconstructing the magnetopause from the data subsets corresponding to these conditions.

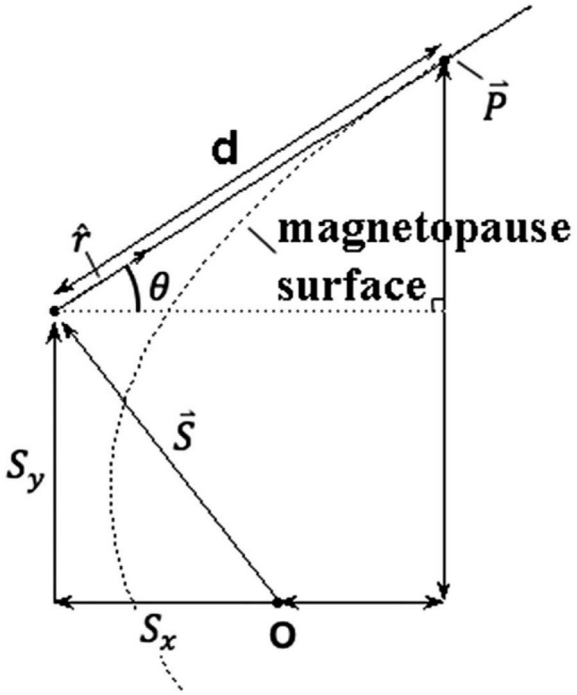

Fig. 3 Reconstruction geometry variables for the derivation of the general formula for the reconstruction of magnetopause from the spacecraft position, $\vec{s}$, parameterized by tangent angle, θ (Figure adapted from Collier and Connor (2018))

Boundary fitting approach (BFA)

Jorgensen et al. (2019a) developed an method to extract the large-scale structures such as the magnetopause, and the bow shock from the soft X-ray images by fitting parameterized models to the images, so we called it boundary fitting approach (BFA). The models consist of a boundary model used for the magnetopause and the bow shock and a emission model used for the regions between the boundaries. The boundary model is a generalization of the model by Shue et al. (1997) and has the following form:

$$r(\theta,\phi) = \frac{r_y(\theta) r_z(\theta)}{\sqrt{[r_z(\theta) cos\phi]^2 + [r_y(\theta) sin\phi]^2}}, \tag{2}$$

where in accordance with Shue et al. (1997),

$$r_y(\theta) = r_0 \left(\frac{2}{1+cos\theta}\right)^{\alpha_y}, \tag{3}$$

and

$$r_z(\theta) = r_0 \left(\frac{2}{1+cos\theta}\right)^{\alpha_z}, \tag{4}$$

where θ is the angle to the X-axis and ϕ is the azimuthal angle in a right-hand sense around the X-axis starting from the Y-axis.

The emissions model consists of three regions separated by the magnetopause and bow shock, both represented by the above equation with different parameters r_0, α_y, and α_z for each. The three regions are the solar wind region sunward (+X) of the bow shock boundary; the magnetosheath between the bow shock and the magnetopause, and the magnetosphere inside the magnetopause. The model is as follows:

$$F(\vec{r}) = \begin{cases} 0 & \text{inside MP} \\ (A_1 + Bsin^8\theta)(\frac{r}{r_{ref}})^{-(\alpha+\beta sin^2\theta)} & \text{between MP and BS} \\ A_2(\frac{r}{r_{ref}})^{-3} & \text{outside BS.} \end{cases} \tag{5}$$

The images used in the fit are then computed from the analytical model based on Eq. 5 for the soft X-ray emissions and Eq. 2 for each of the magnetopause and bow shock. The cost function is the mean-absolute deviation

$$e = \frac{1}{N}\sum_{i=1}^{N} |f_{i,model} - f_{i,data}|, \tag{6}$$

because it typically produces better results (in the sense that it looks like a better fit to the eye) than the least-squares fit when the model and data are not exact matches. For finding the cost-function minimum, the the simplex approach by Nelder and Mead (1965) has been used. Since it is not a global minimization algorithm, the starting point for the minimizer should be carefully picked. The 11 parameters ($A_1, B, \alpha, \beta, A_2, r_0^{mp}, \alpha_y^{mp}, \alpha_z^{mp}, r_0^{bs}, \alpha_y^{bs}$, and α_z^{bs}) are varied until an optimal match with a minimum cost function has been reached.

In the same way as above, we simulate the SWCX soft X-ray emissions by running the global MHD model, namely PPMLR (Hu et al. 2007; Wang et al. 2013). Figure 5a shows a simulated noise-free image, whereas Fig. 5b–d shows the same image with average pixel count rates of 1, 0.1, and 0.01 counts, assuming Poisson statics. The simulated image can be used to mimic the soft X-ray observations from SMILE. The fitted images from the boundary model and emission model are shown in Fig. 6. Comparing the images in Fig. 6 with those in Fig. 5 suggests that this is a close fit for the region imaged.

Jorgensen et al. (2019a, b) also discussed the effect of photon noise and model-fitting noise when extracting the 3D structures from 2D images by applying this boundary fitting approach. It is found that the reconstruction accuracy depends on pixel counts as expected. At lower

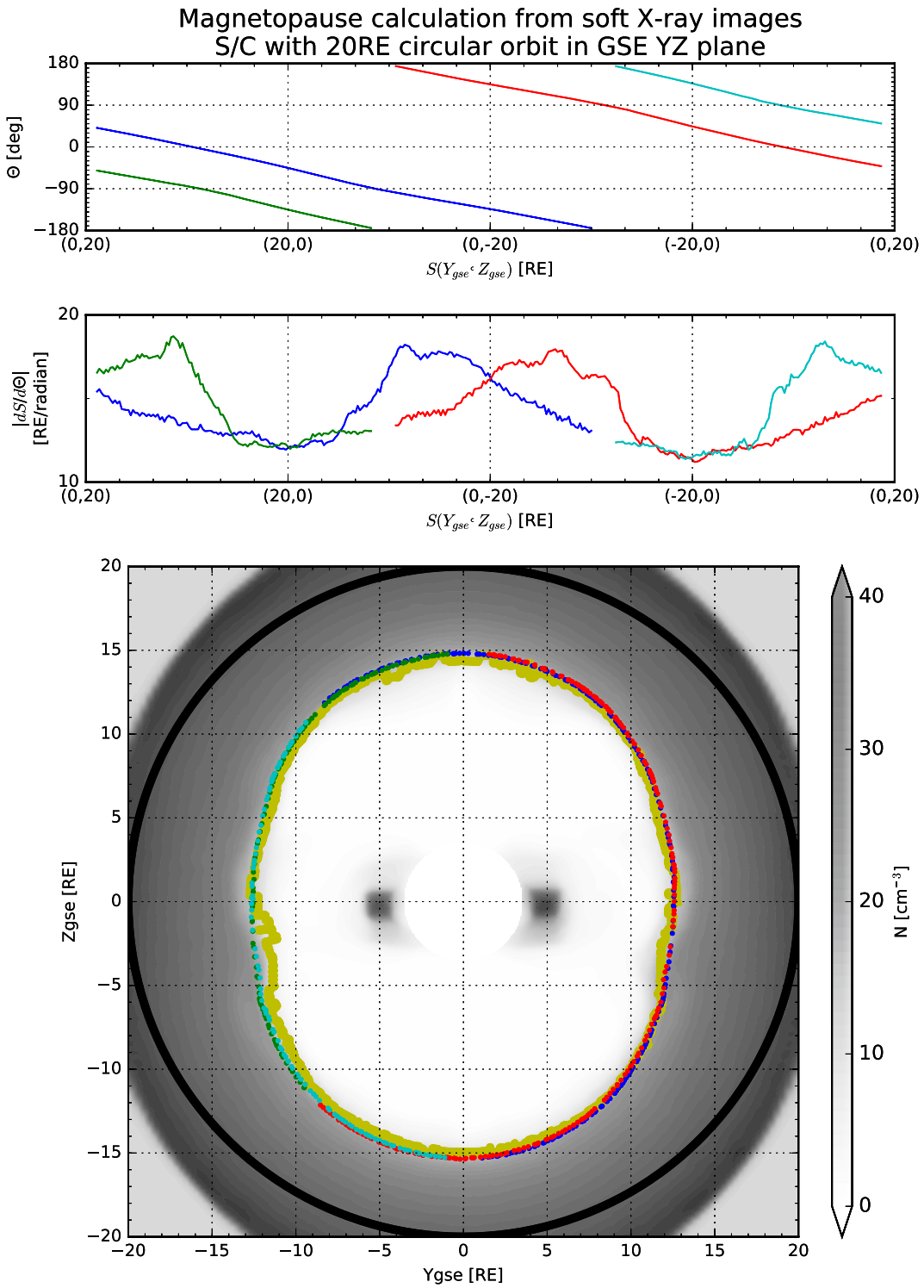

Fig. 4 Reconstruction of the magnetopause. Application of the magnetopause reconstruction algorithm for a circular orbit in the GSE XZ plane (Figure adapted from Collier and Connor (2018))

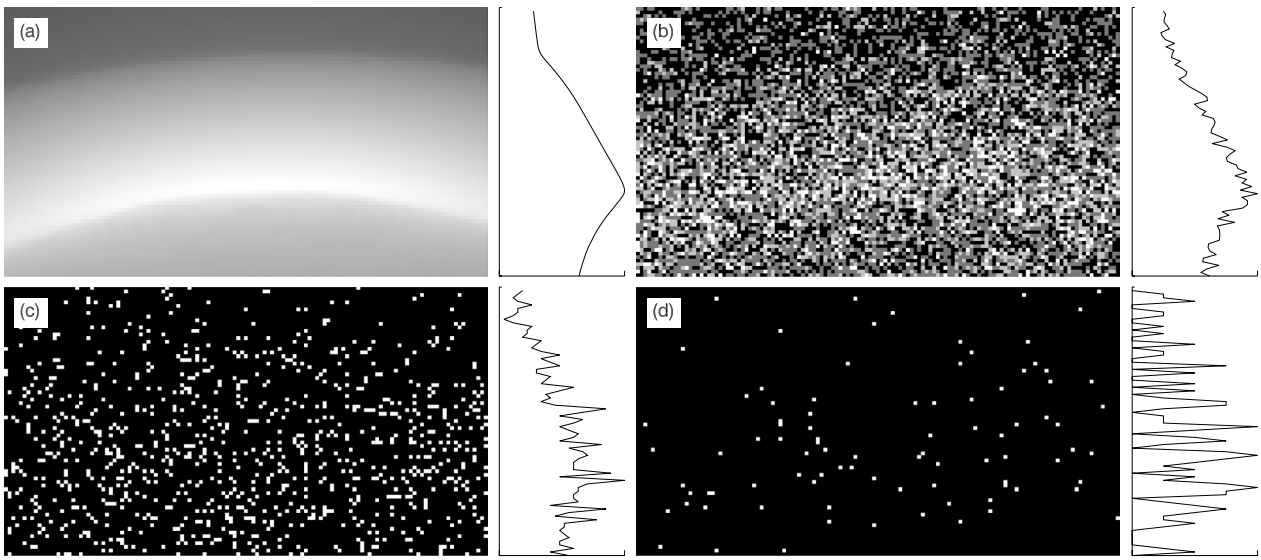

Fig. 5 Simulated soft X-ray images. Simulated images of soft X-ray images from the MHD model with dimensions 75 by 129 pixels. **a** Noise-free image, **b** image with average 1 photon per pixel, **c** 0.1 photons per pixel, and **d** 0.01 photons per pixel, assuming Poisson statistics. The curve on the right side of each image is the horizontal integral of the photons (Figure adapted from Jorgensen et al. (2019a))

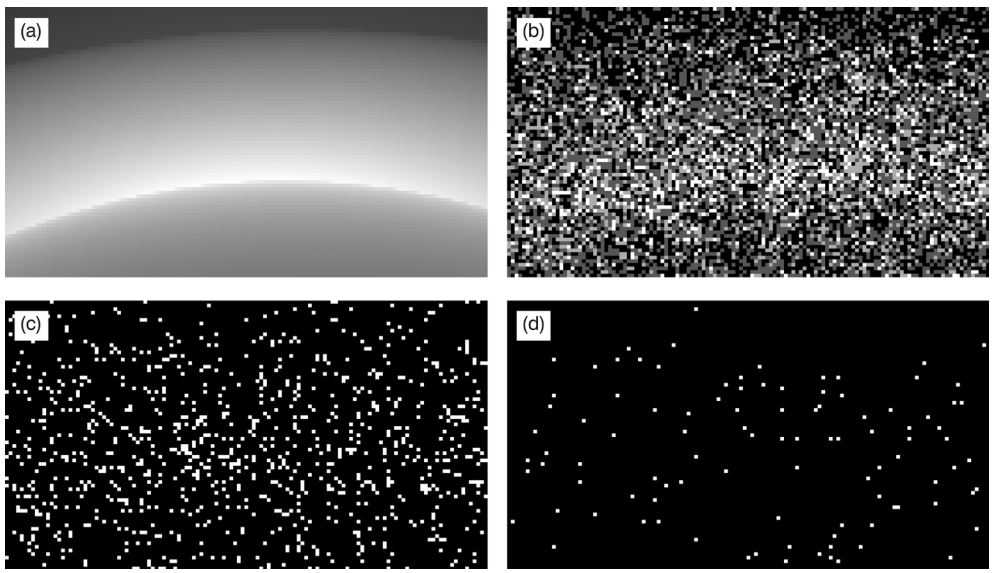

Fig. 6 Fitted soft X-ray images. Fitted images of soft X-ray images in the same format as Fig. 5 (Figure adapted from Jorgensen et al. (2019a))

count rates, the uncertainty becomes higher. The uncertainties obtained depend on viewing geometries. Generally, the more of a boundary that is contained in the image, the smaller the uncertainty on the parameters of that boundary. The fitted model parameters do not vary much with the viewing geometry except when the FOV misses essential elements such as the subsolar point of the magnetopause and bow shock.

In future work, it is worthwhile to consider other functional forms for the boundaries as well as the emission distribution in the magnetosheath and to a less extend

the emission distribution in the solar wind. The emission from the cusps should be also taken into account.

Tangent fitting approach (TFA)

Combining the advantages of TDA and DFA, Sun et al. (2020) developed a new method to derive the 3D magnetopause from a single X-ray image. The basic idea is similar to BFA in Jorgensen et al. (2019a, b) as introduced above, which compares the information provided by the X-ray image as well as a parameterized magnetospheric system in order to find the best match. However, instead of comparing the X-ray intensity at each pixel inside the FOV, TFA compares the tangent directions of the magnetopause. Specifically, as the first step, tangent directions of the magnetopause are derived by finding the location with maximum intensity of the X-ray image (Collier and Connor 2018). For the second step, a parameterized functional form for the magnetopause has been assumed, providing a set of reasonable magnetopause profiles. For each profile, the tangent directions can be calculated numerically. Finally, the magnetopause is reconstructed by finding the best match of the tangent directions analyzed from the soft X-ray image and the magnetopause function. In the second step, the functional form of magnetopause used by Sun et al. (2020) is also the modified Shue et al. (1997) model, shown by Eqs. (2)–(4). By changing r_0, α_y, and α_z within reasonable ranges, a set of magnetopause profiles can be obtained.

TFA has also been validated by using PPMLR-MHD simulation. Figure 7a is the simulated soft X-ray image

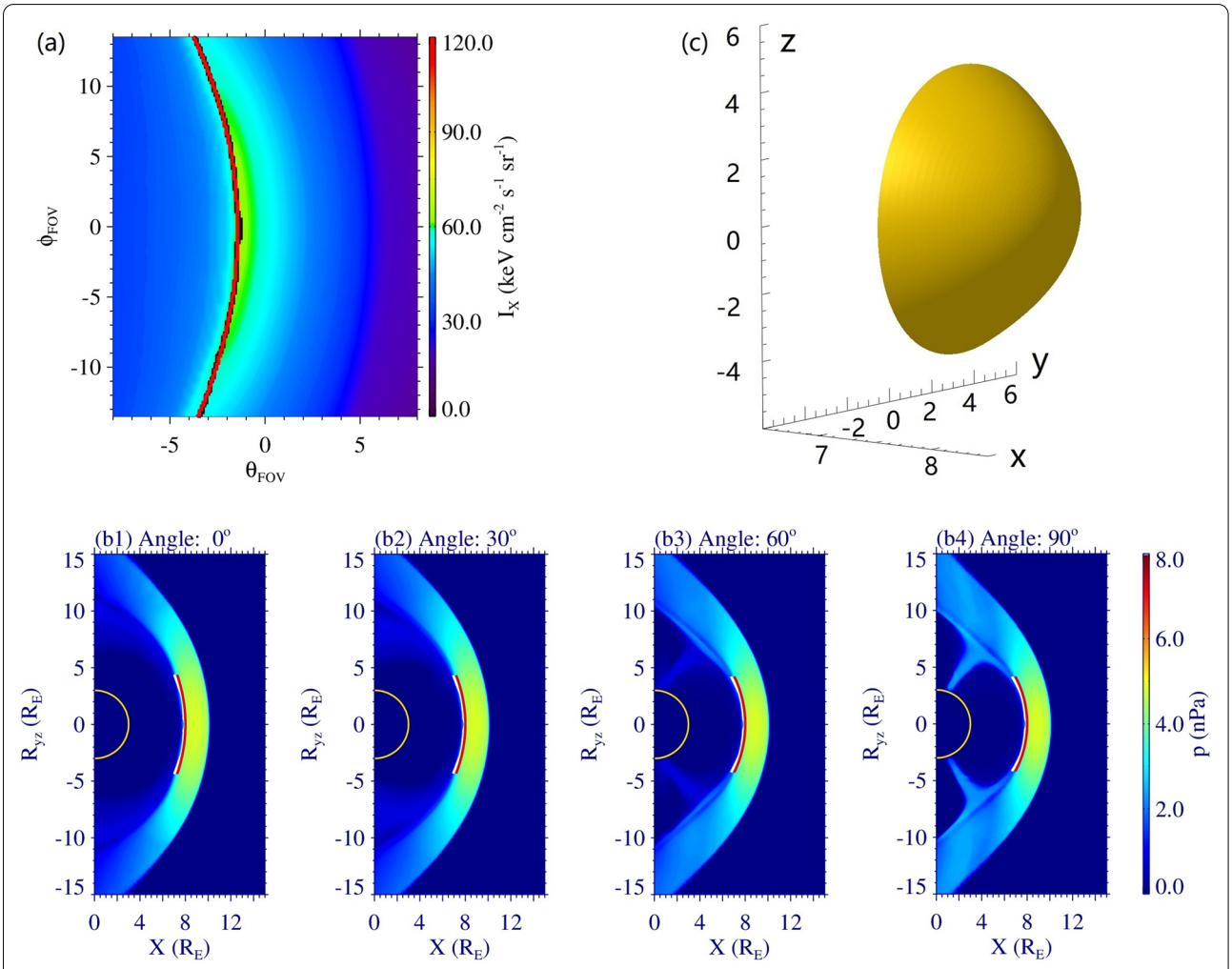

Fig. 7 Validation of TFA using MHD simulations. **a** The simulated soft X-ray image 'observed' by SMILE; **b** the reconstructed magnetopause; **c** 2D views of the reconstructed magnetopause are in red curves, along with the original MHD boundary in white curves. Contours show plasma thermal pressure in planes rotating around the x-axis by 0°, 30°, 60 °, and 90 °, respectively, with 0° indicating the equatorial plane (Figure adapted from Sun et al. (2020))

'observed' by a hypothetical X-ray telescope, with a typical viewing geometry designed for SMILE. By searching for the maximum intensity, the black curve is derived and marked to show the tangent directions of the magnetopause. The tangent directions are also calculated for each possible magnetopause profile, by allowing the three parameters (r_0, α_y, and α_z) in the magnetopause function to float within reasonable ranges. Then the optimum match with the black curve has been found and plotted as the red curve. The parameters corresponding to the red curve are: $r_0 = 8.0\ R_E$, $\alpha_y = 0.8$ and $\alpha_z = 0.2$, which help to portray the reconstructed magnetopause in Fig. 7c. To better evaluate the TFA result, 2D views of the reconstructed magnetopause are marked in Fig. 7(b1)–(b4) by the red curves, in comparison with the original MHD boundary shown by the white curves. The reconstruction result is in good accordance with the MHD boundary.

TFA is further validated with different viewing geometries on a candidate SMILE orbit. It is concluded that there is no apparent orbital bias while utilizing TFA to derive the 3D magnetopause position, as all the three variables show reasonable agreement with the MHD result. Nevertheless, the fitting error tends to increase while the satellite gets closer to the magnetopause boundary as expected. Since it is not able to obtain tangent directions from a point inside the magnetopause, TFA becomes invalid after the satellite enters the magnetosphere.

Based on TFA, we are able to derive the 3D magnetopause position from a single X-ray image, and therefore, TFA is applicable to events under fast solar wind variations. TFA only requires the assumption of the magnetopause function, and thus the number of free variables is apparently reduced compared to that in BFA, which has 11 parameters from the magnetopause, bow shock and magnetosheath emissivity models. Therefore, TFA tends to avoid possible false minima caused by inaccurate initial guess of the parameters. The application of TFA does not rely on simultaneous solar wind observations, which is used to provide well evaluated initial conditions.

Computerized tomography approach (CTA)

Tomography refers to the cross-sectional imaging of an object from either transmission or reflection data collected by illuminating the object from many different directions. The impact of this technique in diagnostic medicine has been revolutionary. Computed tomography (CT) allows physicians to view internal organs noninvasively and scientists to evaluate compound materials non-destructively (Kak and Slaney 1987). The fundamental principle of X-ray CT is to reconstruct an object from its known line integrals or projection. CT image reconstruction algorithms have been extensively studied (see e.g., Kak and Slaney 1987 for a book description). In the field of space research, CT technique was first applied to image the electron density distribution in the ionosphere (Austen et al. 1988). Li et al. (2009) proposed using this method to reconstruct the global density of Earth plasmasphere from the line integrals of the EUV radiation. SMILE will record a large enough number of images from different viewing geometries, so the CT technique may be applicable if the magnetosphere remains unchanging which requires constant solar wind conditions. This is rare in the real situations. However, we could take superposed-epoch approach using images widely spaced in time but for similar solar wind conditions and dipole tilts.

Jorgensen et al. (2022) conducted a theoretical study of the tomographic reconstruction of the magnetosheath X-ray emissions, with $0.125 R_E$ spatial resolution. Generally,

$$A\bar{u} = \bar{p}, \tag{7}$$

where $\bar{u}$ of length n represents the real soft X-ray emission, $\bar{p}$ of length m is the imaged soft X-ray data, denoting all of the pixels in all of the images, and A is the system matrix with m rows and n columns which may be determined by the data collection geometry of the X-ray sensor. Tomographic reconstruction then solves the inverse problem of determining $\bar{u}$ from $\bar{p}$ given a known geometry matrix A. One of the earliest and simplest reconstruction techniques is the Algebraic Reconstruction Technique (ART) (Gordon et al. 1970). The main idea of ART is to make the estimated image satisfy one equation at a time. At each iteration, k, cycling through the rays, $i \in [1; m]$ and the next emissions distribution, $\bar{u}^{k+1}$ is computed as:

$$\bar{u}^{k+1} = \bar{u}^k + \lambda_k \frac{p_i - \overline{A}_i \cdot \bar{u}^k}{\| \overline{A}_i \|^2} \overline{A}_i^T, \tag{8}$$

where $\overline{A}_i$ is now i of A. p_i is the measured data from the ith soft X-ray image. $\bar{u}^k$ is the estimation of the image by the kth iteration.

For many practical cases the ART procedure is nonetheless capable of producing an adequate reconstruction of the original volume distribution, with 180° full coverage. However, for more complex volume distributions, when there is noise present in the images, or to improve the accuracy of the reconstruction with partial angular coverage, additional constraints can be introduced. Jorgensen et al. (2022) employs a denoising algorithm called total variation (TV) minimization which can reduce the total pixel-to-pixel variation in the image (Rudin et al. 1992). The TV algorithm is run after every pixel in every image has been visited in the ART algorithm.

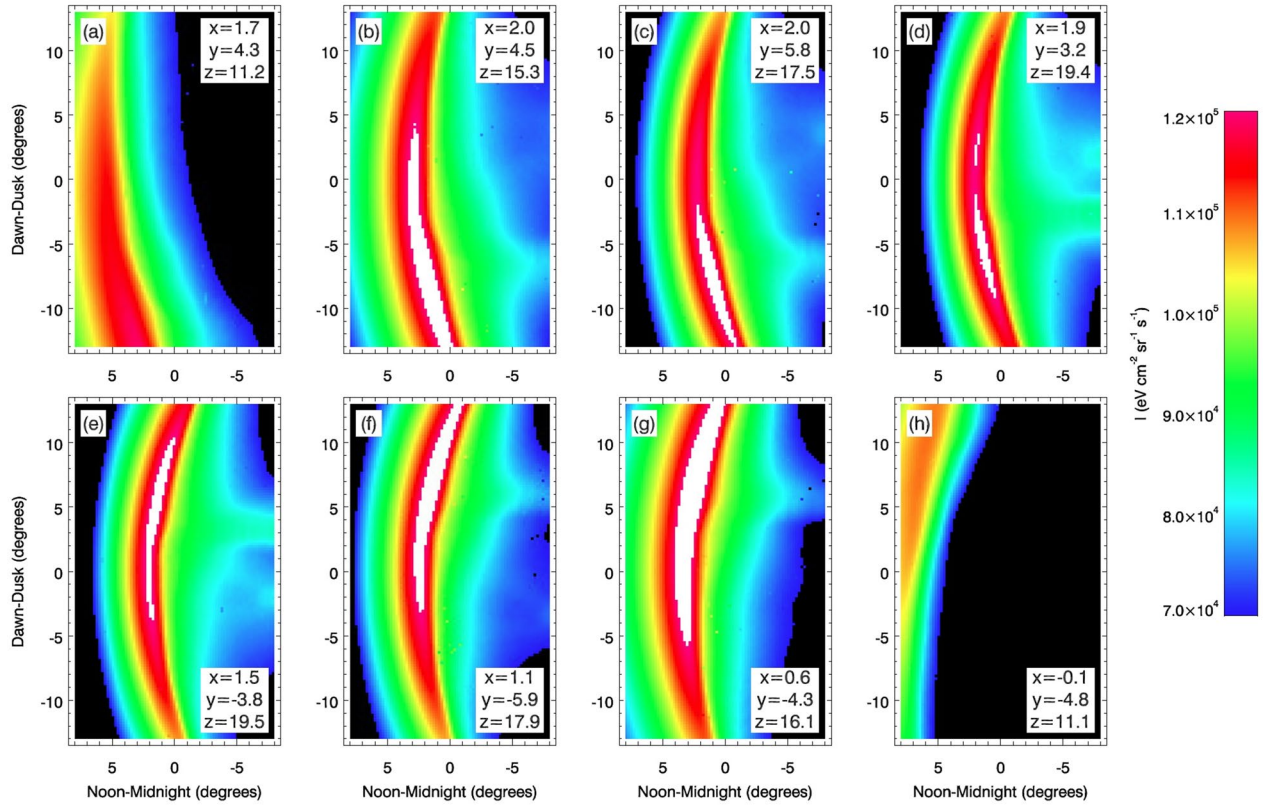

Fig. 8 Simulated soft X-ray images. Simulated soft X-ray images of the emissions from MHD results for a nominal geometric factor and integration time for the apogee pass of SMILE (Figure adapted from Jorgensen et al. (2022))

In the same way as described above, the MHD simulation results are used to mimic the realistic soft X-ray emissions for a nominal designed orbit of SMILE. Figure 8 shows examples of images for a modeled apogee pass of the SMILE spacecraft not long after launch. Figure 9 shows the reconstruction using 100 images with ART and TV. The magnetosheath is reconstructed and that a portion of the cusp is reconstructed as well. As expected, the resulting reconstruction show much less pixel-to-pixel variation with more times TV iteration. Jorgensen et al. (2022) also compared the reconstruction with 10 images and 1000 images, and concluded that 100 images is sufficient for proper reconstruction.

Concluding remarks

The interaction between the solar wind and the Earth's magnetosphere, and the geospace dynamics that result, act as fundamental drivers of space weather. Remote sensing of the magnetosheath and the cusps with soft X-ray imaging is now possible thanks to the relatively recent discovery of solar wind charge exchange (SWCX) X-ray emission. The ESA–CAS joint SMILE (Solar wind Magnetosphere Ionosphere Link Explorer) mission, scheduled to be launched in 2024–2025, will carry a Soft X-ray Imager (SXI) to map the SWCX soft X-ray emission. It is vital to reconstruct the large-scale structures such as the magnetopause, cusps or bow shock from the soft X-ray images, in order to understand the interaction modes and dynamics, to establish quantitatively the input of the solar wind energy into the magnetosphere.

Four approaches have been developed to derive the 3-D magnetopause position from soft X-ray images so far, namely the tangential direction approach (TDA), boundary fitting approach (BFA), tangent fitting approach (TFA), and computerized tomography approach (CTA). The above approaches can be applied to derive the magnetopause under different situations, forming an arsenal of reconstruction techniques. Table 1 presents a brief summary of these reconstruction approaches (also see Figure 4 of Sun et al. 2020).

For any kind of imaging processes, loss of information due to the LOS integration is inevitable. Therefore, it is impossible to derive the 3D configuration from a single 2D image without making any hypotheses. If the reconstruction process can be performed based on

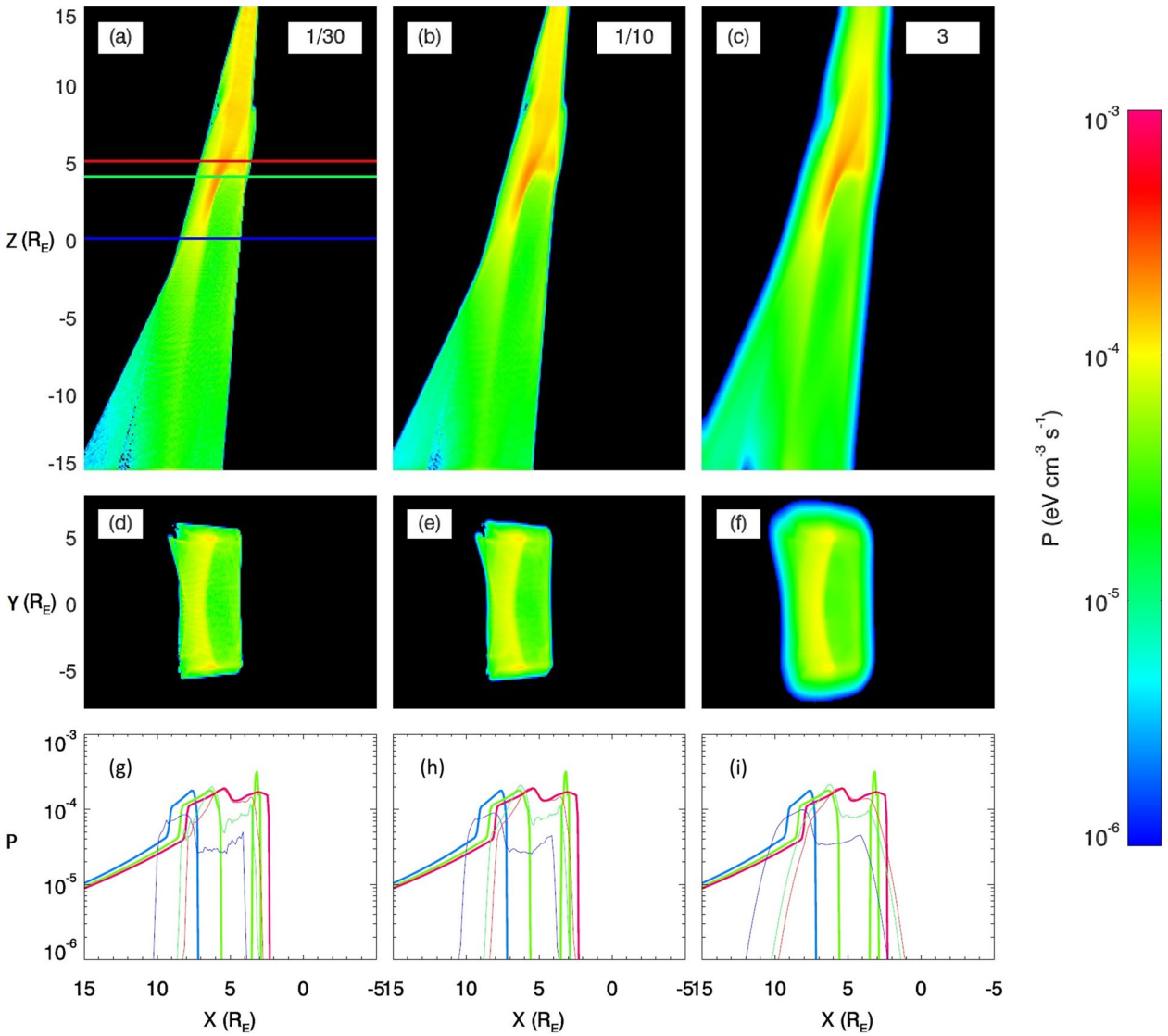

Fig. 9 Reconstruction using 100 images with ART and TV. Reconstruction using 100 images with ART and TV, for different number of TV iterations. The top row (panels **a**–**c**) shows cuts along the *XZ* plane at $Y = 0$, the middle row (**d**–**f**) shows cuts along the *X*–*Y* plane at $Z = 0$, and the bottom row presents the linear cuts at the lines with $Y = 0$ and $Z = 0$ (blue), $Z = 4$ (green), and $Z = 5$ (red) parallel to the *X*-axis. The thin/thick curves are reconstructed/MHD results. The first to third columns are results for 1, 3, 90 TV iterations every 30 ART iterations, respectively (Figure adapted from Jorgensen et al. (2022))

a large set of images, it is possible that very few or no assumptions are required. But if the reconstruction is based on a single image, reasonable assumptions are necessary. Each reconstruction approach is the balance between the required information and the given assumptions. As long as the set of images are taken for the same magnetopause profile, the magnetopause surface can be derived by using CTA basically without additional hypotheses. Applying CTA to more than 30 images will return reasonable reconstruction results according to Jorgensen et al. (2020), and 100 images is sufficient for proper reconstruction. With the same assumption, i.e., the time stationary, TDA can also be used to derive the 3D magnetopause from a set of X-ray images. An additional assumption is that the direction with maximum X-ray intensity is in the tangent direction, which is well demonstrated by the MHD simulations (Collier and Connor 2018). If the number of the analyzed images decreases to 2, the tangent points on the magnetopause viewing from the X-ray telescope are derived by TDA. Reconstructions can also be performed based on a single image, utilizing TFA and

Table 1 Summary of magnetopause reconstruction methods

Approach name	Number of images needed	Assumptions
Boundary fitting approach, BFA (Jorgensen et al. 2019a)	1 image	Functional forms of boundaries and X-ray emissivity
Tangent fitting approach, TFA (Sun et al. 2020)	1 image	1) Functional forms of boundaries
Tangential direction approach, TDA (Collier and Connor 2018)	$\geq$ 2 images	1) Time stationarity
Computerized tomography approach, CTA (Jorgensen et al. 2022)	Many images	Time stationarity

BFA. In addition to the fact that tangent directions align with the directions with maximum X-ray intensity, it is also supposed that the magnetopause surface can be described by a parameterized functional form in order to perform TFA. BFA further assumes the functional forms of the distribution of X-ray emissivity and the shape of bow shock. These additional assumptions provide additional information such as the distribution pattern of the X-ray emissivity in the magnetosheath.

Nevertheless, each approach has its scope of application. CTA and TDA do not rely on assumptions of the magnetopause profile, and thus do not require any prior or empirical knowledge of the magnetopause morphology. But as both approaches obtain information from more than one image, they require the magnetospheric system does not change significantly while taking those images. Parameters that can affect the state of the magnetosphere include the solar wind conditions, dipole tilt angle, ionospheric conductance, etc. Therefore, CTA and TDA can be used to reconstruct the 3D magnetopause during periods with prolonged steady solar wind. If provided with a large database of X-ray images, it is also possible to bin the images according to similar solar wind conditions and dipole tilt before applying CTA or TDA. Compared to CTA, the number of images used by TDA can be reduced to 2, which makes it applicable to a wider range of situations. But less information is gained considering that the tangent points, instead of the 3D magnetopause, are derived. During the intervals with fast solar wind variations, it is desirable to know the instantaneous response of the magnetopause, and thus reconstructions based on a single image is essential. TFA and BFA are applicable to such situations. However, both approaches rely on an empirical description of the magnetospheric system, as they assume function form(s) for structure(s) in the system. Fortunately, statistical studies on the basis of the in situ satellites or numerical simulations provided the prior knowledge of basic morphologies. Reasonable functional forms can thus be assumed. Compared to BFA, the number of variables in TFA is apparently reduced, and therefore, TFA is able to avoid false minima related to the initial guess. As a result, TFA is applicable to situations without simultaneous solar wind observations, while BFA requires the knowledge of solar wind condition enabling a carefully selected initial guess. BFA is an approach that makes the most of information from an X-ray image, as it compares the intensity at each pixel, in comparison with TDA and TFA which studies the directions with maximum intensity. It provides more information (including distribution of X-ray emissivity), but it also risky to be dependent on the assumed distribution pattern which is less well understood. Both TDA and TFA become invalid while the satellite is inside the magnetosphere, where tangent directions do not exist.

Therefore, it is suggested to choose an appropriate method depending on the studies to be performed (time variations of solar wind, available images for the studies, region on the magnetopause to be studied, etc). Quantitative comparison of the reconstructed magnetopause using the four methods will be presented in followed-up studies. Finally, all the four approaches tend to be applicable to the bow shock and further provide additional information about the bow shock position. It is also noted that these four approaches are not limited to the soft X-ray images, and they have a broader application to remote sensing data, such as EUV images or energetic neutral atom (ENA) observations.

Acknowledgements
This work was supported by NNSFC Grants 41731070, 42188101, 42074202, 41774173, in part by the Specialized Research Fund for State Key Laboratories of China, and by the Strategic Pioneer Program on Space Science of CAS Grants XDA15052500, XDA15350201, QYZDJ-SSW-JSC028. TRS is also supported by the Youth Innovation Promotion Association (Y202045).

Author contributions
CW is responsible for the organization and writing of this review paper. TRS developed some approaches to identify the location of the magnetopause from the soft X-ray images, and helped with the comparison and discussion of different approaches. Both authors read and approved the final manuscript.

Declarations

Competing interests
The authors declare that they have no competing interests.

Author details
[1]State Key Laboratory of Space Weather, National Space Science Center, CAS, Beijing, China. [2]School of Earth and Planetary Science, University of Chinese Academy of Sciences, Beijing, China.

Received: 18 April 2022 Accepted: 27 July 2022
Published online: 23 August 2022

References

Akasofu S-I (1985) Explosive magnetic reconnection - Puzzle to be solved as the energy supply process for magnetospheric substorms? Eos Trans Am Geophys Union. https://doi.org/10.1029/EO066i002p00009
Austen JR, Franke SJ, Liu CH (1988) Ionospheric imaging using computerized tomography. Radio Sci 23:288–307
Collier MR, Connor HK (2018) Magnetopasue surface reconstruction from tangent vector observations. J Geophys Res Space Phys 123:10189–10199. https://doi.org/10.1029/2018JA025763
Collier MR, Porter FS, Sibeck DG, Carter JA, Chiao MP, Chornay D et al (2012) Prototyping a global soft X-ray imaging instrument for heliophysics, planetary science, and astrophysics science. Astronomische Nachrichten 333(4):378–382
Collier MR, Snowden SL, Sarantos M, Benna M, Carter JA, Craven TE et al (2014) On lunar exospheric column densities and solar wind access beyond the terminator from ROSAT soft X-ray observations of solar wind charge exchange. J Geophys Res Planets 119:1459–1478. https://doi.org/10.1002/2014JE004628
Cravens T (1997) Comet Hyakutake X-ray source: charge transfer of solar wind heavy ions. Geophy Res Lett 24(1):105–108
Cravens TE (2000) Heliospheric X-ray emission associated with charge transfer of the solar wind with interstellar neutrals. Astrophys J 532:L153–L156
Cravens TE, Robertson IP, Snowden SL (2001) Temporal variations of geocoronal and heliospheric X-ray emission associated with the solar wind interaction with neutrals. J Geophys Res 106:24883–24892
Gordon R, Bender R, Herman GT (1970) Algebraic reconstruction techniques (art) for three-dimensional electron microscopy and x-ray photography. J Theor Biol 29(3):471–481
Hu Y, Guo X, Wang C (2007) On the ionospheric and reconnection potentials of the Earth: Results from global MHD simulations. J Geophys Res 112:A07215. https://doi.org/10.1029/2006JA012145
Jorgensen AM, Sun T, Wang C, Dai L, Sembay S, Wei F et al (2019a) Boundary detection in three dimensions with application to the SMILE mission: The effect of photon noise. J Geophys Res Space Phy. https://doi.org/10.1029/2018JA025919
Jorgensen AM, Sun T, Wang C, Dai L, Sembay S, Zheng JH, Yu XZ (2019b) Boundary detection in three dimensions with application to the SMILE Mission: The effect of model-fitting noise. J Geophys Res Space Phys. https://doi.org/10.1029/2018JA026124
Jorgensen AM, Xu R, Sun T, Huang Y, Li L, Dai L, Wang C (2022) A theoretical study of the Tomographic reconstruction of magnetosheath X-ray emissions. J Geophys Res Space Phys. https://doi.org/10.1029/2021JA029948
Kak AC, Slaney M (1987) Principles of Computerized Tomographic Imaging. IEEE, Piscataway, NJ
Li L, Chen ZQ, Xu RL, Kang KJ, Zhang L, Xing YX (2009) A study of the plasmasphere density distribution using computed tomography methods from the EUV radiation data. Adv Space Res 43:1143–1147
Nelder JA, Mead R (1965) A simplex method for function minimization. The Computer Journal 7(4):308–313
Raeder J, Larson D, Li W, Kepko EL, Fuller-Rowell T (2008) OpenGGCM simulations for the THEMIS mission. Space Sci Rev 141(1–4):535–555. https://doi.org/10.1007/s11214-008-9421-5
Rudin LL, Osher S, Fatemi E (1992) Nonlinear total variation based noise removal algorithms. Physica D 60(1–4):259–268
Russell CT (2000) The solar wind interaction with the Earth's magnetosphere: a tutorial. IEEE Transcations on Plasma Science 28(6):1818–1830. https://doi.org/10.1109/27.902211
Shue J-H, Chao J, Fu H, Russell C, Song P, Khurana K, Singer H (1997) A new functional form to study the solar wind control of the magnetopause size and shape. J Geophys Res 102(A5):9497–9511
Sibeck DG, Allen R, Aryan H et al (2018) Imaging plasma denstiy structures in the soft X-rays generated by solar wind charge exchange with neutrals. Space Sci Rev 214:79. https://doi.org/10.1007/s11214-018-0504-7
SMILE science study team (2018) SMILE (Solar Wind Magnetosphere Ionosphere Link Explorer) Definition Study Report, ESA/SCI
Sun TR, Wang C, Connor HK, Jorgensen A, Sembay S (2020) Deriving the magnetopause position form the soft X-ray image by using the tangent fitting approach. J Geophys Res Space Phys 125:e2020JA028169. https://doi.org/10.1029/2020JA028169
Wang C, Branduardi-Raymont (2018) Progress of Solar Wind Magnetosphere Ionosphere Link Explorer (SMILE) Mission. Chin J Space Sci 38(5):657–661
Wang C, Guo XC, Peng Z et al (2013) Magnetohydrodynamics (MHD) numerical simulations on the interaction of the solar wind with the magnetosphere: A review. Sci China Earth Sci 56:1141–1157. https://doi.org/10.1007/s11430-013-4608-3
Wilson LB III, Brosius AL, Gopalswamy N, Nieves-Chinchilla T, Szabo A, Hurley K et al (2021) A Quarter Century of Wind Spacecraft Discoveries. Rev Geophys 59:e2020RG000714. https://doi.org/10.1029/2020RG00071

Publisher's Note